ACS Photonics

pubs.acs.org/journal/apchd5

Article

Coherent Emission in the Vicinity of 10 THz due to Auger-Suppressed Recombination of Dirac Fermions in HgCdTe Quantum Wells

Sergey V. Morozov, Vladimir V. Rumyantsev,* Maksim S. Zholudev, Alexander A. Dubinov, Vladimir Ya. Aleshkin, Vladimir V. Utochkin, Mikhail A. Fadeev, Konstantin E. Kudryavtsev, Nikolay N. Mikhailov, Sergey A. Dvoretskii, Vladimir I. Gavrilenko, and Frederic Teppe

Cite This: https://doi.org/10.1021/acsphotonics.1c01111

Read Online

ACCESS | Metrics & More | Article Recommendations

ABSTRACT: The discovery of Dirac fermions in a number of 2D and 3D materials boosted the solid-state research in an unprecedented way. Among the many hopes of using their exceptional physical properties, it has been argued that their reduced nonradiative losses would allow graphene to compete with quantum cascade lasers (QCLs) in the race for terahertz (THz) emitters. Unfortunately, the nonradiative Auger recombination (AR) process is still active for massless fermions in gapless graphene. However, for massive Dirac fermions, AR can be entirely suppressed below a certain threshold of the carrier's kinetic energy that depends on the nonparabolicity and the symmetry of the electron and hole dispersions. In this work, by finely tuning the band structure of HgCdTe quantum wells hosting massive Dirac fermions, we set the electronic system below this threshold and demonstrate that the carrier recombination is purely radiative. A coherent interband emission reaching 9.6 THz, that is to say outside the spectral range of current QCLs, is measured under these conditions, opening the way to lossless interband THz emitters.

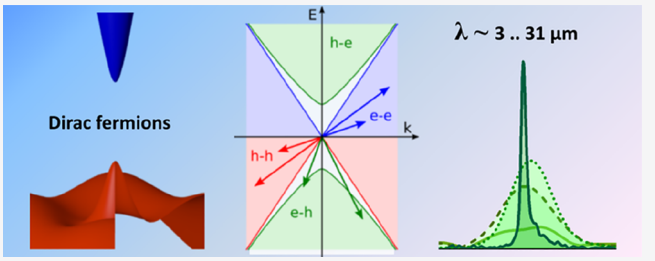

KEYWORDS: *narrow gap materials, Auger recombination, carrier lifetime, stimulated emission, terahertz radiation, long-wavelength lasers*

INTRODUCTION

After the Nobel Prize of 2010 that revealed the groundbreaking prospects of graphene,[1] there has been an increasing interest in the peculiar physical properties of massless quasi-particles in solids, like Dirac,[2] Kane,[3,4] and Weyl[5,6] fermions, recently discovered in a number of 2D and 3D materials. Aside from a wide variety of physical phenomena ranging from high-temperature superconductivity to topological insulators,[2] it appears that Dirac fermions in solids have also a strong card to play for the new generation of light sources. Given its very narrow or even zero gap, Dirac matter is a natural choice for emitters in the terahertz (THz) frequency range. This region of the electromagnetic spectrum has a major application interest for environmental monitoring, nondestructive testing, medicine, security, and many more. Despite a great international research effort for decades, there still remains a lack of compact and efficient laser sources allowing these spectroscopy tasks. Unfortunately, the probability of the radiative transitions decreases at low energy. Therefore, interband THz emission of carriers in narrow gap materials is usually hindered by much faster nonradiative processes. Even though the probability of radiative recombination (RR) increases as the square (n^2) of the concentration of excess carriers n, it is also counteracted by nonradiative Auger recombination (AR). The electron−hole annihilation energy can indeed be transferred to a third charge carrier, and since three particles are involved in this Auger process, its rate increases as n^3, dominating the carrier lifetime at high carrier densities. On the other hand, it is well known that relativistic dispersion provides a unique possibility of suppressing AR. Indeed, when the electron−hole pair recombines and the released energy is carried away by the third particle, the energy and momentum conservation laws must be fulfilled. It turns out that for hyperbolic bands, it is not possible to increment the carrier momentum k and energy E in the intraband transition by the same amount as in the interband transition. In other words, the interband (e−h) and intraband (e−e, h−h) transition "vectors" cannot be collinear in the phase space (k, E), as shown in Figure 1. Indeed, the right part of Figure 1 readily shows that the interband "vector" would always

Received: July 22, 2021

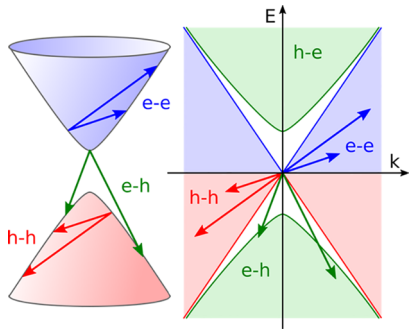

Figure 1. Suppression of AR for massive Dirac fermions. The left part of the figure shows an example of the interband (e−h) and intraband (e−e and h−h) carrier transitions within hyperbolic bands. The right part presents the loci of all possible interband (green areas) and intraband (red and blue areas) transitions in the phase space (k, E). Energy-momentum conservation laws require the e−h vector to be collinear with either the e−e or h−h vector, which is not possible. No intersection occurs between the interband and intraband transition loci, thus forbidding the AR.

have a higher tilt angle (relative to the horizontal axis) than the asymptote, while the intraband "vectors" lie below the asymptote. When discussing the relativistic dispersion, graphene is the first to come to mind; however, in the view of the above, the gapless material is not the best option because it allows aligning of the interband and intraband transitions at the asymptote. Indeed, despite the fact that THz gain was recently demonstrated in graphene,[7−10] there is still some debate regarding the efficiency of AR for the marginal case of massless Dirac fermions.[11,12] In particular, it was suggested that carrier heating[12] and corrugation of the band spectrum[13] can compromise the suppression of AR in graphene, which is strongly correlated with the graphene crystal quality of imperfection. Recent experimental results demonstrate suppression of AR to the level of occurrence of carrier population inversion in an optically pumped epitaxial graphene on a SiC substrate.[14]

In this regard, materials with narrow band gaps, making it possible to approach the graphene dispersion law but leaving a finite gap, are therefore of particular interest. Massive Dirac electrons and tiny band gaps are naturally obtained in semiconductor systems when band inversion is possible, like in ternary alloys PbSnSe,[15] PbSbTe,[16] BiSeIn,[17] and HgCdTe[3] or quantum wells (QWs) and superlattices based on InAs/GaSb[18,19] or HgTe/CdHgTe[20,21] heterostructures. In this work, we explore the interband recombination of Dirac fermions in HgCdTe epitaxial structures by THz photoluminescence (PL), by stimulated emission (SE) measurements, and by time-resolved photoconductivity (PC) measurements.

CARRIER RECOMBINATION

Although AR suppression and THz emission can be studied in other materials with Dirac energy spectra like InAs/GaSb[22] QWs or PbSnSe(Te)[23] alloys, we choose HgCdTe because it combines a number of advantages:

(i) the flexibility of the energy spectrum and the tunability of the band gap with temperature, hydrostatic pressure, or chemical composition; (ii) a well-developed growth technology providing epitaxial structures over a very wide range of parameters, thanks to a low lattice mismatch between CdTe and HgTe; (iii) a low defect/impurity density; (iv) spatially direct optical transitions in QW heterostructures; and (v) direct gap at the Γ point.

The structures under study were grown on GaAs(013) substrates with ZnTe and CdTe buffers[24] using molecular beam epitaxy (MBE) with in situ ellipsometric control of the layer composition and thickness.[25] This growth method has been shown to provide high-quality structures and has been investigated in a large number of works.[3,4,26,27] The details of the growth procedure can be found in ref 24. Samples were cleaved from the as-grown wafer to have a typical size of 5 × 5 mm^2. No special postgrowth treatment was applied to the samples. Due to a peculiar growth direction (013), the cleaved facets do not form the Fabri−Perot resonator, and therefore only single-pass amplification of light was studied.

To probe the carrier density relaxation, we performed a time-resolved study of the PC decay. Figure 2a gives the PC kinetics

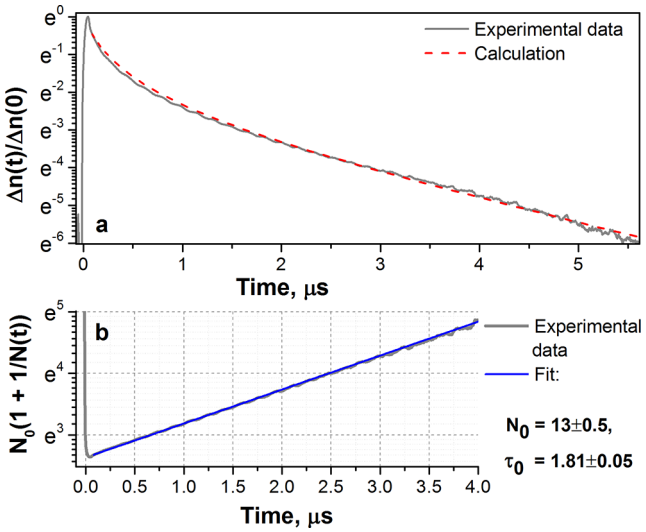

Figure 2. (a) Dynamics of carrier density in the structure S1 at 77 K obtained from PC decay after exciting with a 7 ns pulse of radiation at 8.5 μm. The vertical axis is in the natural logarithmic scale. The dashed line gives the calculated kinetics for RR with the initial carrier density 1.5 × 10^{11} cm^{-2}. (b) Reciprocal function of the experimental data with the offset subtracted and the corresponding exponential fit.

measured in a 3.2 nm-wide HgTe/Cd$_{0.6}$Hg$_{0.4}$Te QW (structure S1, see Table 1 for details) after exciting the PC with a short (7 ns) pulse of radiation at 8.5 μm. The PC curve is strongly nonexponential since the carrier density generated by the pumping pulse is much higher than the dark concentration of carriers as it is revealed below. The nonexponential portion of dynamics can be shown to be entirely due to RR in a very simple way.

Basically, the RR lifetime is inversely proportional to the carrier density[28]

$$\tau_{RR} = \frac{B}{(n_0 + p_0 + \Delta n)}$$

where n_0, p_0 are the equilibrium concentrations of electrons and holes, respectively, and Δn is the excess carrier density generated by the optical excitation. By solving the resulting equation of carrier concentration dynamics after the excitation pulse

$$\frac{dn}{dt} = -\frac{\Delta n}{\tau_{RR}}$$

https://doi.org/10.1021/acsphotonics.1c01111
ACS Photonics XXXX, XXX, XXX−XXX

Table 1. Parameters of the Structures under Study: D_{clad}—Thickness of the Waveguide Layer (Grown on CdTe Buffer from the Substrate Side), x_{wg}, x_{bar}—Cd Content in Waveguide Layers and Barriers, Respectively (x-values are Defined as in $Hg_{1-x}Cd_xTe$), d_{well}—Thickness of QWs, E_g—Band gaps of Structures Calculated in the Framework of Kane 8 × 8 Model for T = 8 K in Units of cm^{-1} and SE Wavelength at 8 K

sample# label	D_{clad} (μm)	x_{wg}	x_{bar}	x_{QW}	d_{well} (nm)	N	E_g@8 K calculated (cm^{-1})	SE wavelength @8 K (μm)
S1	2	0.6 ± 0.02	0.58 ± 0.01	0 ± 0.005	3.2	5	980	10.2
S2	5.2	0.6 ± 0.02	0.66 ± 0.01	0.08 ± 0.01	7.4	5	660	14
S3	9	0.75 ± 0.02	0.7 ± 0.01	0.065 ± 0.005	7.9	15	320	31
S4	9	0.71 ± 0.02	0.61 ± 0.02	0.073 ± 0.005	7.4	15	410	23.6
S5	7.53	0.68 ± 0.02	0.66 ± 0.01	0.08 ± 0.005	7.8	5	480	20.3
S6	8.1	0.65 ± 0.02	0.63 ± 0.02	0.102 ± 0.01	6.1	5	890	10.9
S7	8.1	0.65 ± 0.02	0.63 ± 0.02	0.108 ± 0.01	6.1	5	930	10.4

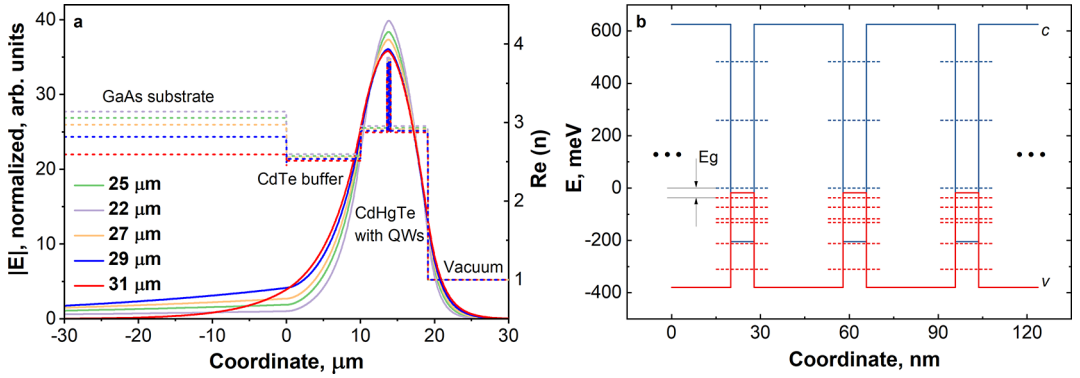

Figure 3. (a) Distribution of the refractive index (dashed lines) and TE_0 mode electric field (solid lines) in structure S3 for the wavelengths near 30 μm. Better confinement is evident for the wavelength of 31 μm, which is closer to the *Reststrahlen* band of the GaAs substrate; (b) conduction band edge (c) and valence band edge (v) diagram over CdHgTe with the QW region in structure S3. The energies in the k = 0 point for several subbands are indicated with dashed lines.

comes the following expression

$$\Delta n(t) = \frac{\Delta n(0)(n_0 + p_0)}{(n_0 + p_0 + \Delta n(0))\exp\left(-\frac{t}{\tau_0}\right) - \Delta n(0)}$$

where $\tau_0 = B/(n_0 + p_0)$ is the RR lifetime for the $\Delta n \ll n_0, p_0$ limit. As can be seen, on the reciprocal scale, the concentration kinetics should have the simple form of an exponential function with offset. By introducing a dimensionless density N and N_0 as

$$N(t) = \frac{\Delta n(t)}{n_0 + p_0}, \qquad N_0 = N(0)$$

we end up with

$$1 + \frac{1}{N(t)} = \left(1 + \frac{1}{N_0}\right)\exp\left(-\frac{t}{\tau_0}\right)$$

Figure 2b shows that the experimental data can be perfectly fitted using this formula. The value N_0 provides the ratio between the initial excess carrier density and the equilibrium one. The dark carrier concentration according to Hall effect measurements lies in the $(1.2-1.5) \times 10^9$ cm^{-2} range. Therefore the excess carrier density at t = 0 can be estimated as $(1.5-2) \times 10^{10}$ cm^{-2}. Using the initial carrier density of 1.5×10^{10} cm^{-2}, a rigorous calculation for the carrier density dynamics, driven only by RR, gives the dashed red line in Figure 1b. Thus, owing to the specific properties of Dirac fermions, one finds no Auger-type contribution to carrier recombination in a QW structure with a band gap as low as ~0.12 eV.

CARRIER SPECTRUM AND LIGHT CONFINEMENT IN STRUCTURES UNDER STUDY

Despite the obvious advantage of AR suppression, it seems that this feature of HgCdTe QWs has remained unexplored until recently. In HgCdTe, the longest lasing wavelength of 5 μm was achieved in 1993 by Arias et al.[29] using thick layers as the active region. Attempts to implement the QW structures have been limited to even shorter wavelengths[30] and have exploited wide QWs, in which the relativistic pattern of the carrier dispersion is not well-pronounced as shown below. Soon after 1994, studies of the interband laser in HgCdTe suffered some setback due to the rapid development of quantum cascade lasers (QCLs). However, though the incumbent QCLs demonstrate excellent performance both in IR and THz regions, they are mainly based on III-V materials and therefore encounter significant problems within the *Reststrahlen* bands of these semiconductors.[31] In particular, QCLs[32,33] are scarce in the "gap" from 5 to 15 THz, yet coherent tunable sources would nevertheless be useful for spectroscopy in this region, offering an alternative to the lead salt lasers.[23,34,35] Nowadays, the progress in MBE makes it possible to reconsider HgCdTe-based structures for THz optoelectronics.[26] SE at wavelengths of up to 20 μm was achieved in HgCdTe QWs in the past years,[36] and gapless HgCdTe bulk crystals have been recently proposed for a Landau level laser operating in the THz range due to suppression of Auger scattering under a magnetic field.[37]

Thanks to the lower frequencies of its optical phonon,[38] HgCdTe should make it possible to cover the spectral region inaccessible for QCLs based on GaAs and InP.[31] In this work, we targeted the 10−15 THz range, and in particular the 32 μm wavelength, which corresponds to the high-frequency edge of

https://doi.org/10.1021/acsphotonics.1c01111
ACS Photonics XXXX, XXX, XXX−XXX

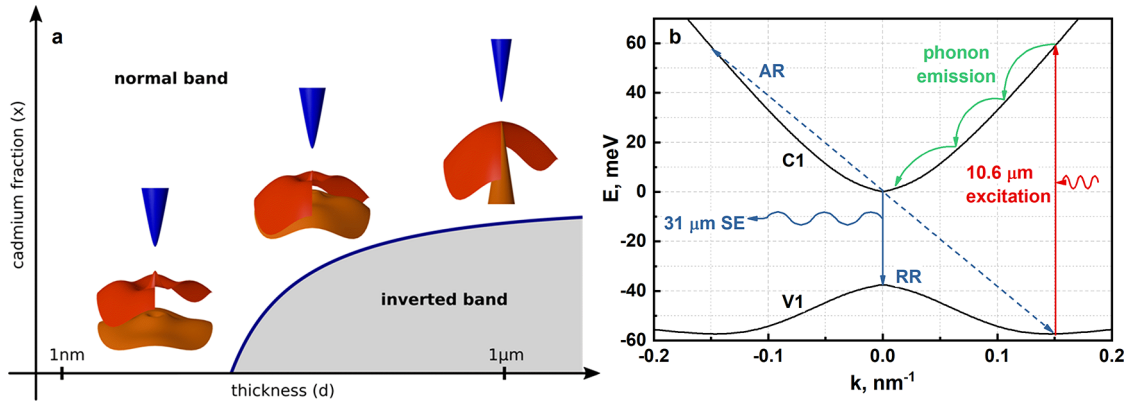

Figure 4. (a) Band structure transformation in the narrow gap $Hg_{1-x}Cd_xTe$ layer sandwiched between $Cd_{0.7}Hg_{0.3}Te$ barriers as the thickness of the layer (d) is reduced from several microns to several nanometers; (b) calculated $E-k$ diagram of structure S3 showing one complete cycle of the optical processes that include optical excitation (absorption), carrier relaxation, and optical emission.

the GaAs *Reststrahlen* band and which has not yet been reached in any QCL. Note that while the proximity of GaAs *Reststrahlen* band is a problem for QCLs, we exploit it to localize the radiation in the vicinity of the active medium. Effective light confinement is indeed a well-known challenge in the long-wavelength region. For wavelengths of around 30 μm, the required thickness of the waveguide layer approaches the limits achievable by MBE. In this study, instead of postgrowth waveguide forming, which might be detrimental for a delicate material such as HgCdTe, we take advantage of the high reflectivity of GaAs in its *Reststrahlen* band. The latter provides the virtual metallization of the substrate when approaching 32 μm and thus allows efficient confinement of the TE mode (Figure 3). The structures contained 5−15 QWs grown inside the dielectric waveguide layer so that the QWs were placed at the TE_0 mode antinode. The QW material corresponds to a zero gap semimetal ($x_{Cd} < 0.168$), but the size quantization effect shifts the confined energy levels so that the QW has a normal band structure, like in a typical semiconductor, when the QW thickness is below the critical one[20] (Figures 3b and 4a). The calculated E_g@8 K in Table 1 shows the energy separation value between the bottom of the lowest conduction subband and the top of the highest valence band.

To understand the idea behind choosing the appropriate QW design, the energy spectra of three HgCdTe structures with the same 40 meV band gap are shown in Figure 4a. The bulk (several μm thick) narrow gap $Hg_{1-x}Cd_xTe$ alloys harbor Kane fermions composed of a double Dirac cone, corresponding to the conduction and light hole bands, and a quasi-flat band corresponding to heavy holes with an effective mass of more than a third of that of a free electron. When the $Hg_{1-x}Cd_xTe$ layer is shrunk down to several nanometers thick QW (with a simultaneous decrease in x to keep a similar band gap), the structure of the valence band is then transformed such that a valley of low-mass holes appears at the $k = 0$ point,[21] surrounded by four side valleys hosting heavier holes.[39] As the QW width is reduced further, the valley at the $k = 0$ point is elevated above the side maxima and becomes symmetrical to the conduction band for a larger range of carrier energy.

In the general case, the net kinetic energy of the three carriers must exceed a certain threshold value for the Auger process to be allowed by the conservation laws.[28,40] The origin of this threshold can be easily understood. A relatively high energy $\sim E_g$ is released when the electron−hole pair annihilates. Therefore, the electron (or hole) remaining in the final state has a momentum large enough to carry such an energy. The net kinetic energy in the initial state is a definite positive function of the momentum, and the initial net momentum has to be equal to that of the final state. Thus, the kinetic energy cannot be arbitrary low, that is, it cannot be less than a certain value energy called the threshold energy. For two parabolic bands characterized by the effective masses m_1 and m_2, this threshold energy can be calculated analytically as

$$E_{th} = \frac{m_1 E_g}{m_1 + m_2}$$

where m_1 corresponds to the mass of the carrier transporting the energy in the Auger process.[40] One can see that in this approximation, the maximum value of the AR threshold realized for symmetrical bands is $E_g/2$. For a strongly nonparabolic energy spectrum, the threshold can considerably exceed the parabolic band limit of $E_g/2$.[41,42] In the general case, the threshold energy can be found numerically or geometrically by plotting the loci of interband and intraband transitions in the (k, E) space, as shown in Figure 1. The threshold of the Auger process corresponds to the intersection of the intraband and interband transition zones. In Figure 1, we can see that such an intersection does not exist for the hyperbolic bands. Therefore, the threshold energy tends to be infinite for relativistic electron−hole dispersion, offering the promising possibility of suppressing AR completely.

In this context, the major effect of the valence band transformation shown in Figure 4 is the dramatic increase in the threshold energy of the AR resulting from the symmetrization and nonparabolicity of the bands in the QW. While in bulk HgCdTe, the heavy hole band entails a negligible AR threshold of $0.008 \times E_g = 0.25$ meV, the semirelativistic dispersion in QWs suppresses AR completely until the hole energy is close enough to the top of the side maxima. The latter allows effectively accumulating the carriers and finally results in SE as shown in Figure 5a,c. The valence band flattening near the side maxima resembles the bulk material, in which the major portion of the threshold energy for the Auger process is introduced by the kinetic energy of the hole. Rigorous calculations of the AR threshold energy demonstrate that the same holds for QW structures under study and the threshold energy is controlled by the side maxima.[43] The dashed lines in Figure 5b,e illustrate how the Auger threshold energy is built up when the side valleys are shifted downward.

https://doi.org/10.1021/acsphotonics.1c01111
ACS Photonics XXXX, XXX, XXX−XXX

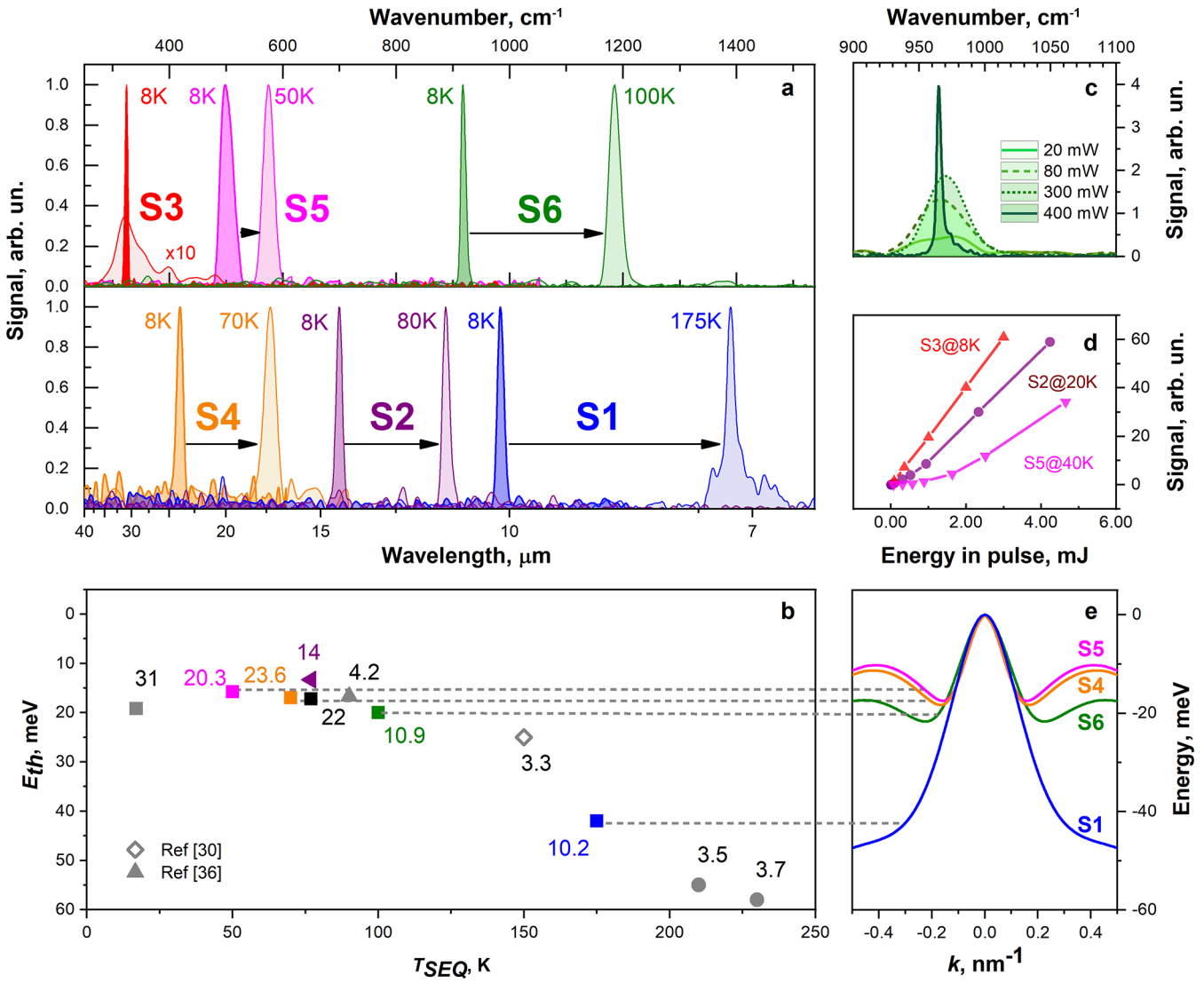

Figure 5. (a) Normalized temperature-driven SE spectra for several structures under study. For structure S3, the PL spectrum is shown for comparison of the linewidths for PL and SE spectra; (b) temperature of SE quenching T_{SEQ} vs the threshold energy of AR E_{th} in HgCdTe QW structures. Labels give the longest SE wavelength obtained from the corresponding structure. The color of a dot corresponds to the energy spectrum of the same color presented in part (e); (c) PL and SE spectra for structure S7 at 8 K under continuous-wave excitation at 900 nm. The legend gives the incident power in a 7 mm diameter spot; (d) SE integral signal vs pulse energy of the exciting CO_2 laser for several structures under study at different temperatures; (e) valence band dispersion for several structures under study. The dashed lines indicate the "critical" hole energy corresponding to the threshold energy of AR. Note that the increase in temperature widens the band gap in the structures under study, which is a remarkable feature of HgCdTe alloys. For this reason, labels in Figure 5b denote the SE wavelength at 8 K, that is, the longest wavelength that was achieved for each structure. One would expect a decrease in T_{SEQ} with increasing SE wavelength, mainly due to free carrier absorption. However, while the SE threshold grows with the wavelength, the change of T_{SEQ} is much weaker if the AR threshold energy is similar. Thus, a longer wavelength results in a decrease in T_{SEQ} only in the group with a similar threshold energy. Consider the structures corresponding to 4.2, 10.9, 14, and 22 μm SE wavelengths, all having the AR threshold energy between 15 and 20 meV and T_{SEQ} in the range 80−100 K. At the same time, structures with similar wavelengths (consider dots at 3.5 μm, 3.7 μm vs 3.3 μm, 10.9 μm vs 10.2 μm, 22 μm vs 20.3 μm) demonstrate quite different T_{SEQ} in agreement with the magnitude of the AR threshold energy.

SE IN STRUCTURES UNDER STUDY: RESULTS AND DISCUSSION

Both from experimental results and the theoretical prediction,[36] it follows that a carrier density of about 10^{11} cm^{-2} is enough to reach the interband gain. Thus, the QW should be designed so that the valley at $k = 0$ could host at least this amount of "relativistic" holes. For structures with a relatively wide gap (SE wavelength ~ 10 μm), the amplification can be achieved using a 900 nm cw laser with a power density as low as 3−10 W/cm^2 (Figure 5c) at 8−15 K or pulsed optical parametric oscillator (OPO) radiation at 2.3 μm for higher temperatures. However, for structures with SE wavelengths longer than 20 μm, short-wavelength excitation results in a large difference between the energy of the exciting photon and the emitted one, which means that the maximum internal quantum efficiency is small and most of the injected optical energy is ultimately converted to heat. Therefore, a pulsed CO_2 laser (10.6 μm) was used for narrower-gap samples.

Note that pumping radiation at 2.3 and 10.6 μm is absorbed only in QWs because the photon energy is not high enough for interband excitation in the barriers. Therefore, the absorption coefficient is only 0.5% per QW, which should be taken into account when considering the quantum efficiency of the SE.

https://doi.org/10.1021/acsphotonics.1c01111
ACS Photonics XXXX, XXX, XXX−XXX

Defined as the ratio of the SE intensity to the absorbed pumping intensity, the photon conversion efficiency reached 2−10% at 8−40 K. Measuring the absolute value of the output quantum efficiency with higher accuracy was complicated because the angular pattern of the emission was not controlled in detail.

Figure 4b shows schematically the processes involved in carrier dynamics within the main subbands for structure S3 as an example. After the excitation with a pumping photon, the carrier loses its kinetic energy by emitting optical phonons with a typical scattering time of 0.1 ps. When the kinetic energy of the carrier does not allow optical phonon emission any more (i.e., less than 15 meV), acoustic phonons can be emitted within the average time of 200 ps for an electron and 10 ps for a hole.[44] These time constants are much shorter than the typical RR lifetime, which lies in the range of 50−100 ns for relevant carrier densities (2×10^9 to 10^{11} cm^{-2}).[43] Thus, after excitation, carriers are rapidly accumulated in the vicinity of the Γ point forming the population inversion. On the other hand, the AR lifetime alters dramatically with carrier density dropping from 10 μs at 5×10^{10} cm^{-2} to 1.6 ns above 3×10^{11} cm^{-2} when the Fermi level enters the side maxima in the valence band. However, the SE onset happens before the carrier density reaches 10^{11} cm^{-2}, for which the AR lifetime is not less than 50 ns. Measuring the output power of emission allows one to estimate the corresponding RR rate after the SE has developed, and in the case of S3, it stands for ∼4 ns slightly above the threshold. Thus, the loss of carriers due to AR is of minor importance up to the onset SE.

Indeed, for the CO_2 laser, the dependence of the integral SE on the pumping intensity (Figure 5d) is well-behaved linear at 8 K and tends to the (0, 0) point, that is, the expected superlinear rise (though actually present) is extremely subtle. The reason is that, given their relativistic properties, the overwhelming majority of holes cannot participate in AR. As a result, before the appearance of SE, recombination is always totally controlled by a radiative (spontaneous) process. Therefore, the quantum efficiency of the outcome emission does not change significantly with the onset of SE, and the latter can be detected mainly by a narrowing of the emission line, as shown in Figure 5c. This is quite typical for the structures under study at low temperatures. The superlinear rise becomes more evident with increasing temperature, when high-energy holes reach side maxima and some loss of carriers occurs via AR. Figure 5d shows the corresponding examples for some of the structures excited with pulsed pumping. The spectrum transformation under pulsed pumping is the same as in Figure 5c and can be followed for relatively wide gap samples, but the PL spectra becomes too noisy compared to cw pumping for narrow gap structures. At low temperatures, PL is weak because the excitation must be low enough to prevent the appearance of SE. At higher temperatures, one can use higher pumping intensities without reaching the SE threshold, but AR is also enhanced and the quantum efficiency of emission below the threshold is consequently lowered. In addition, measurement of the PL spectrum is additionally complicated by the general drop in detector sensitivity in the long-wavelength range and the low repetition rate of 10 Hz available for pulsed pumping.

There are two other factors worth mentioning with regard to obtaining SE as well. The "mexican-hat" like dispersion in the valence band has a peculiar consequence of slowing down the RR at a high carrier density. The holes that occupy the side valleys cannot find the electron counterpart with the same wavevector to recombine radiatively. At the same time, the side valleys have larger density of states due to larger hole mass. The high capacity of the side valleys results in Fermi level pinning in the vicinity of their maxima as the hole density increases. In conjunction with the onset of AR occurring for the holes that are close to the side valleys, it prevents getting a larger gain.

Obviously, filling the states near the side maxima that trigger AR can be achieved not only by increasing the density of the carrier but also by increasing the temperature. Thus, the temperature of SE quenching T_{SEQ}, that is, the temperature above which SE cannot be obtained, becomes a sort of a probe for the threshold energy of AR. Indeed, the set of structures investigated in this work and some previous ones reveals that T_{SEQ} appears to correlate strongly with E_{th}. Figure 5a shows the temperature-driven spectra of SE, and Figure 5b summarizes T_{SEQ} and E_{th} for a number of HgCdTe structures from several works (for structure details, see Table 1).

SE with the longest wavelength of 31 μm is unto itself because the waveguide properties are also strongly temperature-dependent in this case. Indeed, the increase in the band gap induced by the temperature forces the SE wavelength to shift in the range where weaker TE mode localization (see Figure 3) hinders the gain. One could expect SE to recover when the wavelength shortens down to 22−24 μm, but the corresponding temperature of 50−60 K is apparently too high to obtain SE in structure S3.

The experimental studies show that T_{SEQ} cannot be elevated by increasing the pumping intensity, indicating that the gain is limited by extremely fast recombination and/or by carrier heating. Both are naturally introduced by AR. Thus, T_{SEQ} can be considered as the temperature limit at which the AR becomes the overwhelming process controlling the dynamics of the carrier distribution function.

This point is sustained by the time-resolved PC measurements: the PC decay is very well described by AR (dash-dot line in Figure 6) for the S5 structure at 77 K, which is well above T_{SEQ}. This is partly due to a low rate of RR (see the dashed line in Figure 6) that results from the holes filling the side valleys, as it was mentioned earlier. To illustrate this point, Figure 6 also gives

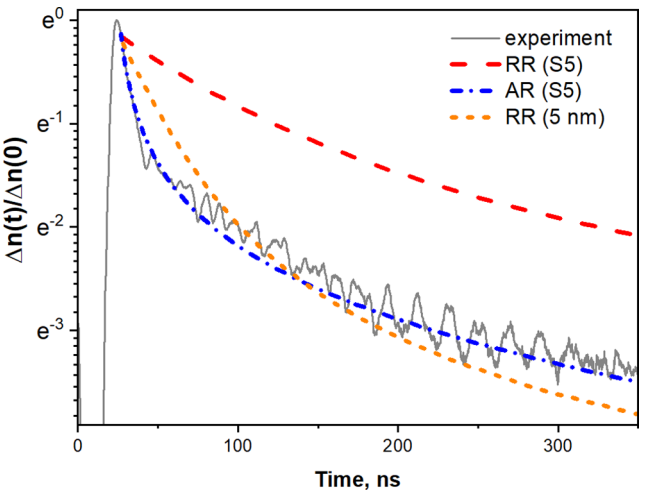

Figure 6. Dynamics of the carrier density in structure S5 at 77 K obtained from PC decay after exciting with a 7 ns pulse of radiation at 9.5 μm. The vertical axis is in the natural logarithmic scale. The dash-dot and dashed lines give the calculated kinetics for AR and RR, respectively, for the initial carrier density 8.25×10^{10} cm^{-2}. The calculated kinetics of carrier density due to RR for a 5 nm thick QW with the same band gap as structure S5 is given as the short dash curve.

https://doi.org/10.1021/acsphotonics.1c01111
ACS Photonics XXXX, XXX, XXX−XXX

the calculated kinetics of carrier density due to RR for a 5 nm thick QW with the same band gap as structure S5. Narrowing of a QW with simultaneous lowering of the Cd content drives the side maxima to lower energy and mitigates the nonmonotonic "mexican-hat" pattern, the same way as for the S1 structure compared to S6 in Figure 5e. As a result, not only the AR threshold increases, but the released holes boost RR. Thus, in narrower QWs, one achieves a more favorable balance between RR and Auger processes.

Aside from tuning the band diagram, improving the waveguide properties is another way to optimize the design for future devices. The main losses below ~30 μm come from mode leaking as well as lattice (multiphonon) absorption in the GaAs substrate. A considerable decrease in the SE threshold is expected for structures with thicker CdTe buffer grown on the substrate before the active part of the structure. As calculations show, the Drude absorption is overcome with a carrier density of only $\sim 5 \times 10^9$ cm^{-2} in the wavelength range less than 30 μm. Lowering the threshold carrier density by increasing the number of QWs in the active region and waveguide optimization would additionally mitigate AR. For wavelengths sufficiently longer than 30 μm, lattice absorption in CdTe becomes important and the carrier density must be increased above 10^{11} cm^{-2} to obtain interband amplification. The corresponding Fermi level position would allow recombination via 2D plasmon emission, suppressed by energy-momentum conservation laws at lower densities. Plasmon emission happens extremely fast, corresponding to a carrier lifetime of ~1 ps at 2×10^{11} cm^{-2}.[43] Though formally plasmon emission is a nonradiative process, it can be used to obtain a highly efficient light source if one provides an appropriate coupling of the plasmon modes to "free space" photons, for example, a metal grating on the surface of the sample. On the other hand, no cladding layers (i.e., photonic waveguide) are needed in the structure for plasmon amplification. Thus, one can exploit two gates to obtain p-type and n-type regions using field effect to form a lateral p-n junction. The gates can be combined with a metal grating that is required to couple the free space radiation to 2D plasmon waves in the QW. This type of structure was also proposed to enhance THz radiation from graphene.[7] Such an approach may be applied to mitigate the well-known problem of p-type doping in HgCdTe diodes, as far as current pumping is concerned. The possibility of the plasmonic gain becomes more and more relevant for structures with a narrower gap since it can deliver giant amplification coefficients ~10^6 cm^{-2}.[26] In a long perspective, exploiting plasmons in HgCdTe QWs seems to be the key to obtain coherent emission in the far-infrared and THz range.[45] The considerations above do not cancel the task of AR suppression since a dramatic carrier heating is introduced even by a moderately slow Auger process. However, above 10^{11} cm^{-2}, the AR rates should be calculated using random phase approximation to account for screening and taking into consideration the nonequilibrium electron−hole distributions, which is beyond the scope of this paper.

CONCLUSIONS

To conclude, we have demonstrated how the semirelativistic energy spectrum of Dirac fermions in narrow-gap HgCdTe QW structures prevents electrons and holes from recombining via the Auger process, thus allowing the band to fill up until the emergence of the SE. A 6-fold increase in the SE wavelength (from 5 to 31 μm) was achieved simply by using relatively narrow QWs instead of bulklike layer as the active medium. It seems that the prospects of this approach are far from exhausted. Thoughtful designing of the band diagrams, also including strain engineering,[46] is the basis for further raising the AR threshold in QWs with an even narrower band gap. In conjunction with the improvement in THz gain due to plasmons,[45] the AR suppression opens up the opportunity to overcome two-phonon absorption in HgCdTe and to go beyond the wavelength of 31 μm achieved in this work. In QWs with a sufficiently high AR threshold E_{th}, carrier recombination is controlled solely by the radiative mechanism, paving the way for efficient interband emitters in the THz/FIR region. Based on the correlation between E_{th} and the maximum operating temperature, one can expect Peltier-cooled operation of interband HgCdTe lasers with an AR threshold energy of about 50 meV achievable in narrow QWs with a low Cd content. These lasers could compete with QCLs, rare in the region of 5−15 THz, thanks to a simpler design and a "natural" wavelength tuning with temperature.

EXPERIMENTAL SECTION/METHODS

Band Diagram Calculation. The calculation method is based on the envelope function approximation.[47] The wavefunction is written as an expansion over a set of functions $u_{n,0}(\mathbf{r})$ with lattice periodicity forming the Kohn-Luttinger basis: $\Psi = \sum_n \mathbf{F}_n(\mathbf{r}) u_{n,0}(\mathbf{r})$ where coefficients $\mathbf{F}_n(\mathbf{r})$ are smooth envelope functions. Thus, the state of the electron is described by the column vector $\mathbf{F}(\mathbf{r}) = \begin{pmatrix} \mathbf{F}_1(\mathbf{r}) \\ \vdots \\ \mathbf{F}_N(\mathbf{r}) \end{pmatrix}$. This vector is calculated as the solution of the stationary Schrodinger equation with the matrix Hamiltonian operator: $\mathbf{H}(\hat{\mathbf{k}},\mathbf{r})\mathbf{F} = E\mathbf{F}$ where quasi-momentum $\hat{\mathbf{k}}$ is a differential operator: $\hat{\mathbf{k}} = -i\nabla$

In the bulk homogeneous sample, the solution is a column of plane waves described by band index n and three-dimensional wavenumber $\mathbf{k}$: $\mathbf{F}_{n,\mathbf{k}}(\mathbf{r}) = \mathbf{C}_{n,\mathbf{k}} e^{i\mathbf{kr}}$ where the coefficients $\mathbf{C}_{n,\mathbf{k}}$ are the solutions of the following equation: $\mathbf{H}_{\mathbf{k}}\mathbf{C}_{n,\mathbf{k}} = E_{n,\mathbf{k}}\mathbf{C}_{n,\mathbf{k}}$

In QWs, two components of quasi-momentum k_x and k_y are conserved, and the envelope function vector has the following form: $\mathbf{F}_{n,kx,ky}(\mathbf{r}) = \mathbf{f}_{n,kx,ky}(z) e^{i(k_x x + k_y y)}$ where coefficients $\mathbf{f}_{n,kx,ky}(z)$ are the solutions of the following equation: $\mathbf{H}_{kx,ky}(\hat{\mathbf{k}}_z, z)\mathbf{f}_{n,kx,ky}(z) = E_{n,kx,ky}\mathbf{f}_{n,kx,ky}(z)$

In our calculations, we use Burt-Foreman approximation[48] for the 8 × 8 Kane Hamiltonian[49] with parameters from ref 49. Since our samples are grown on the crystallographic plane (013), the Hamiltonian is modified accordingly.[50,51] The z-dependent components of the envelope functions are calculated by plane wave expansion.

The model used to calculate the RR rate is described in ref 52, while ref 42 describes how the threshold energies for different Auger processes can be calculated in HgCdTe QW structures.

PL and SE Measurements. PL spectra studies were carried out at T = 8−300 K in a closed-cycle cryostat optically connected to a Bruker Vertex 80v Fourier transform infrared (FTIR) spectrometer. The FTIR spectrometer was operated in the step scan mode. When studying PL, a continuous wave laser was used with excitation wavelength in λ_{exc} = 800−900 nm (Ti/sapphire laser Spectra Physics "Matisse-DR"). Excitation power was varied from 10 to 900 mW. The beam spot at the sample was ~3 mm in diameter.

A special modulation technique was used, which is described in ref 53, with the laser beam mechanically chopped. The modulation frequency was chosen according to the detector response time, typically lying in the 200 Hz−2 kHz range.

https://doi.org/10.1021/acsphotonics.1c01111
ACS Photonics XXXX, XXX, XXX−XXX

Depending on the spectral range of the PL or signal, one of the following detectors was used: liquid N_2-cooled MCT Photovoltaic D317 (range 4800−850 cm^{-1}), MCT/InSb sandwich D318 (range 10,000−600 cm^{-1}), or liquid He-cooled silicon bolometer D211 (range 700−10 cm^{-1}). The detector signal was fed to the Stanford Research System SR560 amplifier and then recovered by a Stanford Research System SR830 lock-in amplifier. The data acquisition by the analog-to-digital converter (ADC) of the FTIR spectrometer was delayed by ∼5 time constants of the lock-in amplifier after each step of the moving mirror of the spectrometer.

For the SE studies, the same measurement setup was used except for the lock-in amplifier. Pulsed optical pumping was provided by either a "SOLAR Laser Systems" KTP OPO emitting 10 ns long pulses at 2.3 μm or a CO_2 laser with 10.6 μm wavelength at 100 ns long pulse. The repetition rate for both sources did not exceed 10 Hz, and therefore, the SE signal from the detector was acquired directly by external high-speed ADC triggered with the synchronization pulse as described in ref 36.

PC Kinetics Study. The PC decay was measured after 7 ns long narrow-band radiation pulses provided by the "SOLAR Laser Systems" OPO with an outcoming wavelength of 8.5 μm. The pulse energy was 10 μJ, and the beam diameter on the sample was 7 mm. Using low-energy quanta for the excitation of PC was exploited to generate "cold" carriers in the vicinity of the $k = 0$ point so that the effects related to the carrier heating were avoided. The PC signal was acquired with a digital oscilloscope "Le Croy" with 1 GHz upper limiting frequency. Thus, the pulse duration limited the time resolution to ∼7 ns. The details on the experimental setup can be found in ref 54.

AUTHOR INFORMATION

Corresponding Author

Vladimir V. Rumyantsev − *Institute for Physics of Microstructures of RAS, Nizhny Novgorod 603950, Russia; Lobachevsky University of Nizhny Novgorod, Nizhny Novgorod 603950, Russia;* orcid.org/0000-0003-0739-2214; Email: rumyantsev@ipmras.ru

Authors

Sergey V. Morozov − *Institute for Physics of Microstructures of RAS, Nizhny Novgorod 603950, Russia; Lobachevsky University of Nizhny Novgorod, Nizhny Novgorod 603950, Russia*

Maksim S. Zholudev − *Institute for Physics of Microstructures of RAS, Nizhny Novgorod 603950, Russia; Lobachevsky University of Nizhny Novgorod, Nizhny Novgorod 603950, Russia*

Alexander A. Dubinov − *Institute for Physics of Microstructures of RAS, Nizhny Novgorod 603950, Russia; Lobachevsky University of Nizhny Novgorod, Nizhny Novgorod 603950, Russia;* orcid.org/0000-0002-0900-8928

Vladimir Ya. Aleshkin − *Institute for Physics of Microstructures of RAS, Nizhny Novgorod 603950, Russia; Lobachevsky University of Nizhny Novgorod, Nizhny Novgorod 603950, Russia*

Vladimir V. Utochkin − *Institute for Physics of Microstructures of RAS, Nizhny Novgorod 603950, Russia*

Mikhail A. Fadeev − *Institute for Physics of Microstructures of RAS, Nizhny Novgorod 603950, Russia; Laboratoire Charles Coulomb, UMR 5221, CNRS-University of Montpellier, Montpellier 34095, France*

Konstantin E. Kudryavtsev − *Institute for Physics of Microstructures of RAS, Nizhny Novgorod 603950, Russia*

Nikolay N. Mikhailov − *Institute of Semiconductor Physics, Siberian Branch of Russian Academy of Sciences, Novosibirsk 630090, Russia; Novosibirsk State University, Novosibirsk 630090, Russia*

Sergey A. Dvoretskii − *Institute of Semiconductor Physics, Siberian Branch of Russian Academy of Sciences, Novosibirsk 630090, Russia; Tomsk State University, Tomsk 634050, Russia*

Vladimir I. Gavrilenko − *Institute for Physics of Microstructures of RAS, Nizhny Novgorod 603950, Russia; Lobachevsky University of Nizhny Novgorod, Nizhny Novgorod 603950, Russia*

Frederic Teppe − *Laboratoire Charles Coulomb, UMR 5221, CNRS-University of Montpellier, Montpellier 34095, France*

Complete contact information is available at: https://pubs.acs.org/10.1021/acsphotonics.1c01111

Notes

The authors declare no competing financial interest.

ACKNOWLEDGMENTS

The work was sponsored by Center of Excellence ≪Center of Photonics≫ funded by The Ministry of Science and Higher Education of the Russian Federation, contract no. 075-15-2020-906)

REFERENCES

(1) Novoselov, K. S.; Geim, A. K.; Morozov, S. V.; Jiang, D.; Katsnelson, M. I.; Grigorieva, I. V.; Dubonos, S. V.; Firsov, A. A. Two-dimensional gas of massless Dirac fermions in graphene. *Nature* **2005**, *438*, 197−200.

(2) Vafek, O.; Vishwanath, A. Dirac Fermions in Solids: From High-Tc Cuprates and Graphene to Topological Insulators and Weyl Semimetals. *Annu. Rev. Condens. Matter Phys.* **2014**, *5*, 83−112.

(3) Teppe, F.; Marcinkiewicz, M.; Krishtopenko, S. S.; Ruffenach, S.; Consejo, C.; Kadykov, A. M.; Desrat, W.; But, D.; Knap, W.; Ludwig, J.; Moon, S.; Smirnov, D.; Orlita, M.; Jiang, Z.; Morozov, S. V.; Gavrilenko, V. I.; Mikhailov, N. N.; Dvoretskii, S. A. Temperature-driven massless Kane fermions in HgCdTe crystals. *Nat. Commun.* **2016**, *7*, 12576.

(4) Orlita, M.; Basko, D. M.; Zholudev, M. S.; Teppe, F.; Knap, W.; Gavrilenko, V. I.; Mikhailov, N. N.; Dvoretskii, S. A.; Neugebauer, P.; Faugeras, C.; Barra, A.-L.; Martinez, G.; Potemski, M. Observation of three-dimensional massless Kane fermions in a zinc-blende crystal. *Nat. Phys.* **2014**, *10*, 233−238.

(5) Jia, S.; Xu, S.-Y.; Hasan, M. Z. Weyl semimetals, Fermi arcs and chiral anomalies. *Nat. Mater.* **2016**, *15*, 1140−1144.

(6) Xu, S.-Y.; Belopolski, I.; Alidoust, N.; Neupane, M.; Bian, G.; Zhang, C.; Sankar, R.; Chang, G.; Yuan, Z.; Lee, C.-C.; Huang, S.-M.; Zheng, H.; Ma, J.; Sanchez, D. S.; Wang, B.; Bansil, A.; Chou, F.; Shibayev, P. P.; Lin, H.; Jia, S.; Hasan, M. Z. Discovery of a Weyl fermion semimetal and topological Fermi arcs. *Science* **2015**, *349*, 613−617.

(7) Yadav, D.; Tamamushi, G.; Watanabe, T.; Mitsushio, J.; Tobah, Y.; Sugawara, K.; Dubinov, A. A.; Satou, A.; Ryzhii, M.; Ryzhii, V.; Otsuji, T. Terahertz light-emitting graphene-channel transistor toward single-mode lasing. *Nanophotonics* **2018**, *7*, 741−752.

(8) Boubanga-Tombet, S.; Chan, S.; Watanabe, T.; Satou, A.; Ryzhii, V.; Otsuji, T. Ultrafast carrier dynamics and terahertz emission in optically pumped graphene at room temperature. *Phys. Rev. B: Condens. Matter Mater. Phys.* **2012**, *85*, 035443.

(9) Boubanga-Tombet, S.; Knap, W.; Yadav, D.; Satou, A.; But, D. B.; Popov, V. V.; Gorbenko, I. V.; Kachorovskii, V.; Otsuji, T. Room-

Temperature Amplification of Terahertz Radiation by Grating-Gate Graphene Structures. *Phys. Rev. X* **2020**, *10*, 031004.
(10) Li, T.; Luo, L.; Hupalo, M.; Zhang, J.; Tringides, M. C.; Schmalian, J.; Wang, J. Femtosecond Population Inversion and Stimulated Emission of Dense Dirac Fermions in Graphene. *Phys. Rev. Lett.* **2012**, *108*, 167401.
(11) Winzer, T.; Malić, E. Impact of Auger processes on carrier dynamics in graphene. *Phys. Rev. B: Condens. Matter Mater. Phys.* **2012**, *85*, 241404.
(12) Alymov, G.; Vyurkov, V.; Ryzhii, V.; Satou, A.; Svintsov, D. Auger recombination in Dirac materials: A tangle of many-body effects. *Phys. Rev. B* **2018**, *97*, 205411.
(13) Golub, L. E.; Tarasenko, S. A.; Entin, M. V.; Magarill, L. I. Valley separation in graphene by polarized light. *Phys. Rev. B: Condens. Matter Mater. Phys.* **2011**, *84*, 195408.
(14) Someya, T.; Fukidome, H.; Watanabe, H.; Yamamoto, T.; Okada, M.; Suzuki, H.; Ogawa, Y.; Iimori, T.; Ishii, N.; Kanai, T.; Tashima, K.; Feng, B.; Yamamoto, S.; Itatani, J.; Komori, F.; Okazaki, K.; Shin, S.; Matsuda, I. Suppression of supercollision carrier cooling in high mobility graphene on SiC(000-1). *Phys. Rev. B* **2017**, *95*, 165303.
(15) Dziawa, P.; Kowalski, B. J.; Dybko, K.; Buczko, R.; Szczerbakow, A.; Szot, M.; Łusakowska, E.; Balasubramanian, T.; Wojek, B. M.; Berntsen, M. H.; Tjernberg, O.; Story, T. Topological crystalline insulator states in $Pb_{1-x}Sn_xSe$. *Nat. Mater.* **2012**, *11*, 1023−1027.
(16) Ferreira, S. O.; Abramof, E.; Motisuke, P.; Rappl, P. H. O.; Closs, H.; Ueta, A. Y.; Boschetti, C.; Bandeira, I. N. Experimental observation of band inversion in the PbSnTe system. *J. Appl. Phys.* **1999**, *86*, 7198−7200.
(17) Brahlek, M.; Bansal, N.; Koirala, N.; Xu, S.-Y.; Neupane, M.; Liu, C.; Hasan, M. Z.; Oh, S. Topological-Metal to Band-Insulator Transition in$(Bi_{1-x}In_x)_2Se_3$Thin Films. *Phys. Rev. Lett.* **2012**, *109*, 186403.
(18) Suchalkin, S.; Belenky, G.; Ermolaev, M.; Moon, S.; Jiang, Y.; Graf, D.; Smirnov, D.; Laikhtman, B.; Shterengas, L.; Kipshidze, G.; Svensson, S. P.; Sarney, W. L. Engineering Dirac Materials: Metamorphic $InAs_{1-x}Sb_x/InAs_{1-y}Sb_y$ Superlattices with Ultralow Bandgap. *Nano Lett.* **2018**, *18*, 412−417.
(19) Krishtopenko, S. S.; Desrat, W.; Spirin, K. E.; Consejo, C.; Ruffenach, S.; Gonzalez-Posada, F.; Jouault, B.; Knap, W.; Maremyanin, K. V.; Gavrilenko, V. I.; Boissier, G.; Torres, J.; Zaknoune, M.; Tournié, E.; Teppe, F. Massless Dirac fermions in III-V semiconductor quantum wells. *Phys. Rev. B* **2019**, *99*, 121405.
(20) Bernevig, B. A.; Hughes, T. L.; Zhang, S.-C. Quantum spin Hall effect and topological phase transition in HgTe quantum wells. *Science* **2006**, *314*, 1757−1761.
(21) Büttner, B.; Liu, C. X.; Tkachov, G.; Novik, E. G.; Brüne, C.; Buhmann, H.; Hankiewicz, E. M.; Recher, P.; Trauzettel, B.; Zhang, S. C.; Molenkamp, L. W. Single valley Dirac fermions in zero-gap HgTe quantum wells. *Nat. Phys.* **2011**, *7*, 418−422.
(22) Krishtopenko, S. S.; Ruffenach, S.; Gonzalez-Posada, F.; Boissier, G.; Marcinkiewicz, M.; Fadeev, M. A.; Kadykov, A. M.; Rumyantsev, V. V.; Morozov, S. V.; Gavrilenko, V. I.; Consejo, C.; Desrat, W.; Jouault, B.; Knap, W.; Tournié, E.; Teppe, F. Temperature-dependent terahertz spectroscopy of inverted-band three-layer InAs/GaSb/InAs quantum well. *Phys. Rev. B* **2018**, *97*, 245419.
(23) Maremyanin, K. V.; Ikonnikov, A. V.; Bovkun, L. S.; Rumyantsev, V. V.; Chizhevskii, E. G.; Zasavitskii, I. I.; Gavrilenko, V. I. Terahertz Injection Lasers Based on a PbSnSe Solid Solution with an Emission Wavelength up to 50 μm and Their Application in the Magneto-spectroscopy of Semiconductors. *Semiconductors* **2018**, *52*, 1590−1594.
(24) Mikhailov, N. N.; Smirnov, R. N.; Dvoretsky, S. A.; Sidorov, Y. G.; Shvets, V. A.; Spesivtsev, E. V.; Rykhlitski, S. V. Growth of $Hg_{1-x}Cd_xTe$ nanostructures by molecular beam epitaxy with ellipsometric control. *Int. J. Nanotechnol.* **2006**, *3*, 120−130.
(25) Shvets, V. A.; Mikhailov, N. N.; Ikusov, D. G.; Uzhakov, I. N.; Dvoretskii, S. A. Determining the Compositional Profile of HgTe/$Cd_xHg_{1-x}Te$ Quantum Wells by Single-Wavelength Ellipsometry. *Opt. Spectrosc.* **2019**, *127*, 340−346.
(26) Ruffenach, S.; Kadykov, A.; Rumyantsev, V. V.; Torres, J.; Coquillat, D.; But, D.; Krishtopenko, S. S.; Consejo, C.; Knap, W.; Winnerl, S.; Helm, M.; Fadeev, M. A.; Mikhailov, N. N.; Dvoretskii, S. A.; Gavrilenko, V. I.; Morozov, S. V.; Teppe, F. HgCdTe-based heterostructures for terahertz photonics. *APL Mater.* **2017**, *5*, 035503.
(27) Gusev, G. M.; Olshanetsky, E. B.; Kvon, Z. D.; Mikhailov, N. N.; Dvoretsky, S. A.; Portal, J. C. Quantum Hall Effect near the Charge Neutrality Point in a Two-Dimensional Electron-Hole System. *Phys. Rev. Lett.* **2010**, *104*, 166401.
(28) Blakemore, J. S. *Semiconductor Statistics*; Pergamon: Oxford, 1962.
(29) Arias, J. M.; Zandian, M.; Zucca, R.; Singh, J. HgCdTe infrared diode lasers grown by MBE. *Semicond. Sci. Technol.* **1993**, *8*, S255−S260.
(30) Bleuse, J.; Bonnet-Gamard, J.; Mula, G.; Magnea, N.; Jean-Louis, P. Laser emission in HgCdTe in the 2−3.5 μm range. *J. Cryst. Growth* **1999**, *197*, 529−536.
(31) Vitiello, M. S.; Scalari, G.; Williams, B.; De Natale, P. Quantum cascade lasers: 20 years of challenges. *Opt. Express* **2015**, *23*, 5167−5182.
(32) Razeghi, M.; Lu, Q. Y.; Bandyopadhyay, N.; Zhou, W.; Heydari, D.; Bai, Y.; Slivken, S. Quantum cascade lasers: from tool to product. *Opt. Express* **2015**, *23*, 8462−8475.
(33) Williams, B. S. Terahertz quantum-cascade lasers. *Nat. Photonics* **2007**, *1*, 517−525.
(34) Shotov, A. P. Tunable diode lasers for 3 to 40 μm infrared spectral region. *AIP Conf. Proc.* **1991**, *240*, 87−94.
(35) Tacke, M.; Elliott, C. T.; Krier, A.; Murdin, B. N. Lead−salt lasers. *Philos. Trans. R. Soc., A* **2001**, *359*, 547−566.
(36) Morozov, S. V.; Rumyantsev, V. V.; Kadykov, A. M.; Dubinov, A. A.; Kudryavtsev, K. E.; Antonov, A. V.; Mikhailov, N. N.; Dvoretskii, S. A.; Gavrilenko, V. I. Long wavelength stimulated emission up to 9.5μmfrom HgCdTe quantum well heterostructures. *Appl. Phys. Lett.* **2016**, *108*, 092104.
(37) But, D. B.; Mittendorff, M.; Consejo, C.; Teppe, F.; Mikhailov, N. N.; Dvoretskii, S. A.; Faugeras, C.; Winnerl, S.; Helm, M.; Knap, W.; Potemski, M.; Orlita, M. Suppressed Auger scattering and tunable light emission of Landau-quantized massless Kane electrons. *Nat. Photonics* **2019**, *13*, 783−787.
(38) Talwar, D. N.; Vandevyver, M. Vibrational properties of HgCdTe system. *J. Appl. Phys.* **1984**, *56*, 1601−1607.
(39) Krishtopenko, S. S.; Teppe, F. Realistic picture of helical edge states in HgTe quantum wells. *Phys. Rev. B* **2018**, *97*, 165408.
(40) Abakumov, V. N.; Perel, V. I.; Yassievich, I. N. *Nonradiative Recombination in Semiconductors*; Elsevier Science Publishers: North-Holland, 1991.
(41) Alymov, G.; Rumyantsev, V.; Morozov, S.; Gavrilenko, V.; Aleshkin, V.; Svintsov, D. Fundamental Limits to Far-Infrared Lasing in Auger-Suppressed HgCdTe Quantum Wells. *ACS Photonics* **2020**, *7*, 98−104.
(42) Aleshkin, V. Y.; Dubinov, A. A.; Rumyantsev, V. V.; Morozov, S. V. Threshold energies of Auger recombination in HgTe/CdHgTe quantum well heterostructures with 30-70 meV bandgap. *J. Phys.: Condens. Matter* **2019**, *31*, 425301.
(43) Aleshkin, V. Y.; Rumyantsev, V. V.; Kudryavtsev, K. E.; Dubinov, A. A.; Utochkin, V. V.; Fadeev, M. A.; Alymov, G.; Mikhailov, N. N.; Dvoretsky, S. A.; Teppe, F.; Gavrilenko, V. I.; Morozov, S. V. Auger recombination in narrow gap HgCdTe/CdHgTe quantum well heterostructures. *J. Appl. Phys.* **2021**, *129*, 133106.
(44) Morozov, S. V.; Joludev, M. S.; Antonov, A. V.; Rumyantsev, V. V.; Gavrilenko, V. I.; Aleshkin, V. Y.; Dubinov, A. A.; Mikhailov, N. N.; Dvoretskiy, S. A.; Drachenko, O.; Winnerl, S.; Schneider, H.; Helm, M. Study of lifetimes and photoconductivity relaxation in heterostructures with $Hg_xCd_{1-x}Te/Cd_yHg_{1-y}$ Te quantum wells. *Semiconductors* **2012**, *46*, 1362−1366.
(45) Kapralov, K.; Alymov, G.; Svintsov, D.; Dubinov, A. Feasibility of surface plasmon lasing in HgTe quantum wells with population inversion. *J. Phys.: Condens. Matter* **2019**, *32*, 065301.

https://doi.org/10.1021/acsphotonics.1c01111
ACS Photonics XXXX, XXX, XXX−XXX

(46) Leubner, P.; Lunczer, L.; Brüne, C.; Buhmann, H.; Molenkamp, L. W. Strain Engineering of the Band Gap of HgTe Quantum Wells Using Superlattice Virtual Substrates. *Phys. Rev. Lett.* **2016**, *117*, 086403.
(47) Luttinger, J. M.; Kohn, W. Motion of Electrons and Holes in Perturbed Periodic Fields. *Phys. Rev.* **1955**, *97*, 869−883.
(48) Foreman, B. A. Elimination of spurious solutions from eight-band k×p theory. *Phys. Rev. B: Condens. Matter Mater. Phys.* **1997**, *56*, R12748−R12751.
(49) Novik, E. G.; Pfeuffer-Jeschke, A.; Jungwirth, T.; Latussek, V.; Becker, C. R.; Landwehr, G.; Buhmann, H.; Molenkamp, L. W. Band structure of semimagnetic $Hg_{1-y}Mn_yTe$ quantum wells. *Phys. Rev. B: Condens. Matter Mater. Phys.* **2005**, *72*, 035321.
(50) Los, J.; Fasolino, A.; Catellani, A. Generalization of the k•p approach for strained layered semiconductor structures grown on high-index-planes. *Phys. Rev. B: Condens. Matter Mater. Phys.* **1996**, *53*, 4630−4648.
(51) Zholudev, M.; Teppe, F.; Orlita, M.; Consejo, C.; Torres, J.; Dyakonova, N.; Czapkiewicz, M.; Wróbel, J.; Grabecki, G.; Mikhailov, N.; Dvoretskii, S.; Ikonnikov, A.; Spirin, K.; Aleshkin, V.; Gavrilenko, V.; Knap, W. Magnetospectroscopy of two-dimensional HgTe-based topological insulators around the critical thickness. *Phys. Rev. B: Condens. Matter Mater. Phys.* **2012**, *86*, 205420.
(52) Aleshkin, V. Y.; Dubinov, A. A.; Rumyantsev, V. V.; Fadeev, M. A.; Domnina, O. L.; Mikhailov, N. N.; Dvoretsky, S. A.; Teppe, F.; Gavrilenko, V. I.; Morozov, S. V. Radiative recombination in narrow gap HgTe/CdHgTe quantum well heterostructures for laser applications. *J. Phys.: Condens. Matter* **2018**, *30*, 495301.
(53) Shao, J.; Lu, W.; Lü, X.; Yue, F.; Li, Z.; Guo, S.; Chu, J. Modulated photoluminescence spectroscopy with a step-scan Fourier transform infrared spectrometer. *Rev. Sci. Instrum.* **2006**, *77*, 063104.
(54) Rumyantsev, V. V.; Morozov, S. V.; Antonov, A. V.; Zholudev, M. S.; Kudryavtsev, K. E.; Gavrilenko, V. I.; Dvoretskii, S. A.; Mikhailov, N. N. Spectra and kinetics of THz photoconductivity in narrow-gap $Hg_{1-x}Cd_xTe$ ($x < 0.2$) epitaxial films. *Semicond. Sci. Technol.* **2013**, *28*, 125007.

https://doi.org/10.1021/acsphotonics.1c01111
ACS Photonics XXXX, XXX, XXX−XXX